Synaptic Plasticity and Visual Memory in a Neuromorphic 2D Memitter Based on WS$_2$ Monolayers

Federico Ferrarese Lupi,* Gianluca Milano,* Angelo Angelini, Mateo Rosero-Realpe, Bruno Torre, Erika Kozma, Christian Martella, and Carlo Grazianetti*

Neuromorphic computing aims to leverage physical phenomena of adaptive materials for emulating information processing capabilities and effectiveness of biological neuronal circuits. In this framework, memristors (resistors with memory) based on 2D materials are demonstrated for the hardware implementation of highly integrated artificial neural networks. All the works reported thus far exploited electrical properties of 2D materials to emulate neuromorphic functionalities. Here, a 2D memitter (emitter with memory) is reported on that exploits the stimuli-responsive photoluminescence of a monolayer WS$_2$ for neuromorphic-type of data processing. A combined experimental and modeling approach reveals that photoluminescent dynamics triggered by optical stimulation emulates Short-Term synaptic Plasticity and Visual Short-Term Memory typical of biological systems. While spatio-temporal processing capabilities of input signals can be used for information processing in the context of reservoir computing, the capability of the 2D memitter of sensing, processing, and memorizing-forgetting optical inputs in the same physical substrate can be utilized for in-sensor computing.

1. Introduction

In the era of Big Data and Artificial Intelligence, neuromorphic systems aiming to mimic the effectiveness of the information processing capabilities of the human brain are nowadays expected to overcome limitations of current computing technologies.[1] Cross-fertilized by progresses in neurosciences, advancements in neuromorphic computing are inherently related to the development of hardware computing architectures based on new device concepts that leverage physical phenomena to emulate bio-inspired functionalities.[2,3] In this framework, neuromorphic architectures based on electronic and optical systems have been demonstrated for hardware implementation of neural networks and brain-inspired computing paradigms beyond von Neumann computing.[4–6] Inspired by biological systems where both sensing and processing of information involve the nervous system, adaptive materials have been proposed also for in-sensor processing information to avoid data transfer between sensors and computing units.[7–9]

Among emerging neuromorphic technologies, devices based on materials that can adapt their response when subjected to external stimulation have been exploited for the emulation of synaptic plasticity effect and neuron functionalities, where information processing capabilities and storage of knowledge rely on the ability of the active material to adapt its internal state depending on the history of the applied stimulation.[2,10,11] In this regard, intriguing properties of 2D materials have been demonstrated to be promising for the development of neuromorphic systems characterized by improved device scaling and possibility of integration with planar wafer technology.[12,13] Besides promising for the realization of ionic-gating-modulated synaptic transistors[14,15] and ferroelectric field-effect transistors for unconventional computing,[16–18] 2D materials have been exploited as active materials for the fabrication of electronic devices termed memristors (i.e., resistors with memory) that are able to emulate typical features of biological synapses.[19–22] For these applications, the fabrication and integration of high-density 2D-CMOS hybrid microchips for memristive technologies have been recently demonstrated,[23] while 2D semiconductor photodiode arrays have been exploited as neural network image sensors.[24] Also, the van der Waals

F. Ferrarese Lupi, G. Milano, A. Angelini, M. Rosero-Realpe
Advanced Materials Metrology and Life Science Division
INRiM (Istituto Nazionale di Ricerca Metrologica)
Strada delle Cacce 91, Torino 10135, Italy
E-mail: f.ferrareselupi@inrim.it; g.milano@inrim.it

The ORCID identification number(s) for the author(s) of this article can be found under https://doi.org/10.1002/adfm.202403158

M. Rosero-Realpe, B. Torre
Department of Applied Science and Technology
Politecnico di Torino
C.so Duca degli Abruzzi 24, Torino 10129, Italy
E. Kozma
CNR-SCITEC
via A. Corti 12, Milano 20133, Italy
C. Martella, C. Grazianetti
CNR-IMM
Agrate Brianza Unit
via C. Olivetti 2, Agrate Brianza 20864, Italy
E-mail: carlo.grazianetti@cnr.it

2403158 (1 of 9)

**ADVANCED
SCIENCE NEWS**

www.advancedsciencenews.com

**ADVANCED
FUNCTIONAL
MATERIALS**

www.afm-journal.de
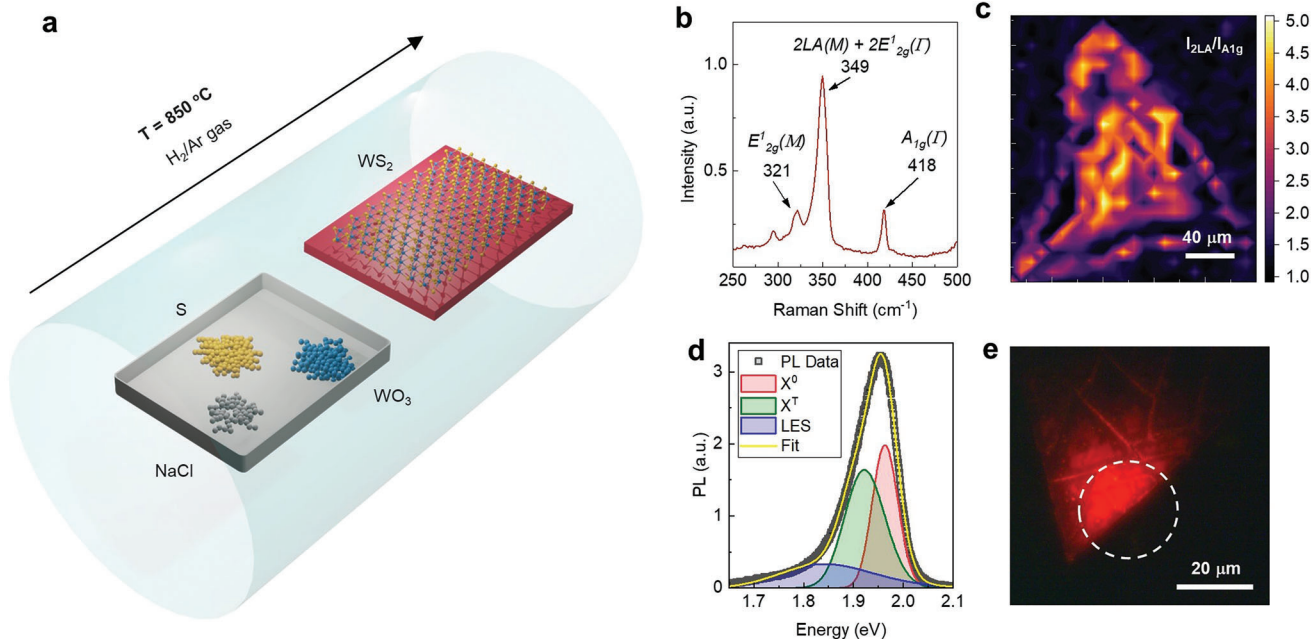
Figure 1. WS$_2$ synthesis and characterization. a) Sketch of the CVD furnace used for the halide-assisted synthesis of WS$_2$ flakes on SiO$_2$ substrates from WO$_3$ and S powders using the seeding promoter PTARG. b) Raman spectrum of a WS$_2$ flake. c) Map of the intensity ratio I$_{2LA}$/I$_{A1g}$. d) PL spectrum of the WS$_2$ (black squared points) and Gaussian peak deconvolution showing the contribution of X^0 (red curve) X$^-$ (green curve) and LES (blue curve). e) Wide field PL image of a portion of WS$_2$ flake, taken in the PL setup described in Figure S4 (Supporting Information). The dashed white circle highlights the full width at half maximum of the excitation beam (see Figure S5, Supporting Information).

semiconductor α-phase indium selenide has been proposed as optoelectronic system emulating synapses where the electrical response of the device can be modulated by both electronic and optical stimulation.[25] Despite the adaptive optical emission has been recently reported to emulate neuromorphic functionalities in phosphorescent materials,[26,27] no previous works reported on the synaptic photoluminescent response of 2D materials thus far. In this context, the ultimate thickness and the optoelectronic properties of 2D materials make them promising for multilevel functions like integrated circuits with high-integration density.[28]
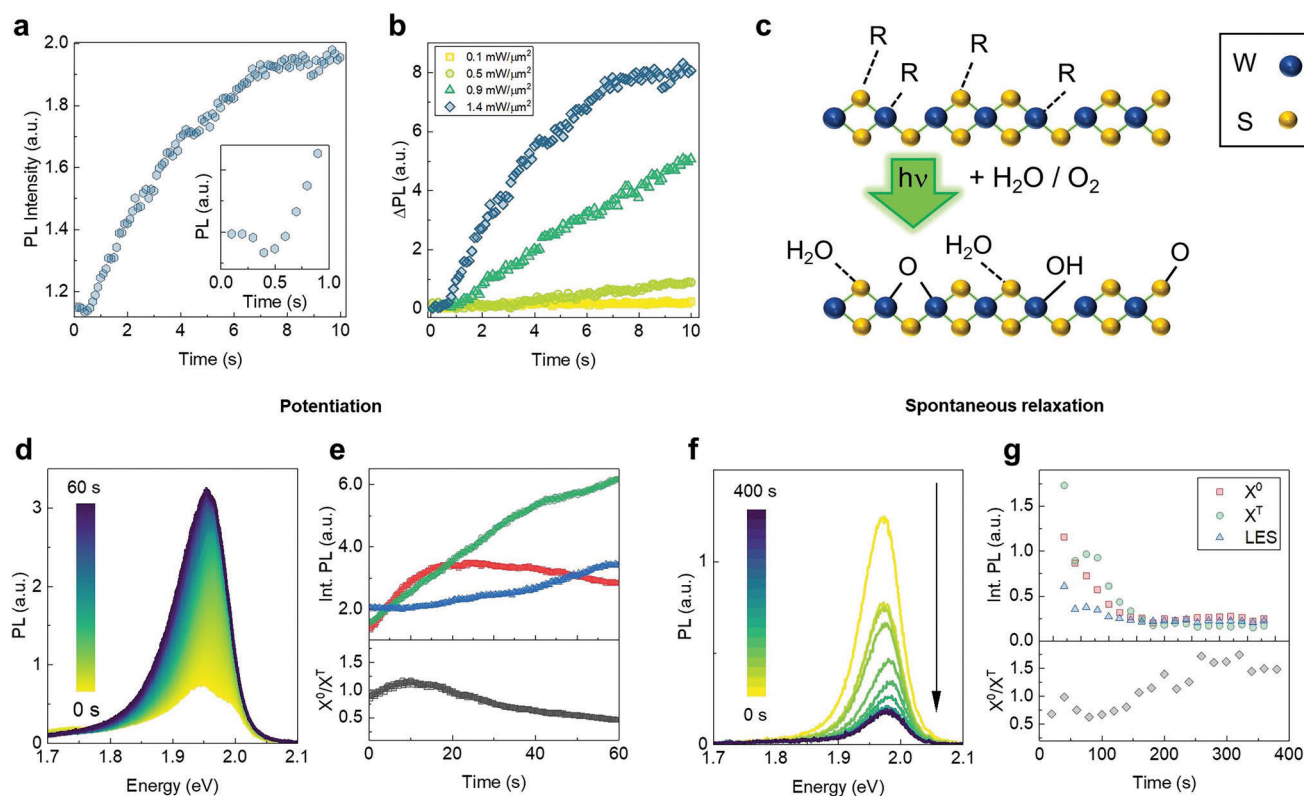
Here, we report on a novel device concept termed "2D memitter" (i.e., emitter with memory) that exploits the stimuli-responsive photoluminescence (PL) of a WS$_2$ monolayer for all-optical neuromorphic-type of data processing. We show that optical stimulation of large-area WS$_2$ flakes provokes a time-dependent PL response under ambient conditions, characterized by highly nonlinear dynamics, fading memory characteristics, and large-area synaptic response. Through an integration of experimental and modeling methodologies, we illustrate the potential for photoemission dynamics to replicate biological functions akin to Short-Term Synaptic Plasticity and Visual Short-Term Memory. In a framework where the future of neuromorphic computing can be closely tied to the integration of various complementary technologies to create intelligent systems, the here reported 2D memitter could serve as a physical platform for processing and short-term optical information storage, complementing existing neuromorphic devices for computation.[29]

2. Results and Discussion

2.1. WS$_2$ Synthesis and Characterization

Triangular shaped flakes of WS$_2$ with lateral size of hundreds of micrometres were obtained by halide-assisted chemical vapor deposition (CVD),[30] using perylene-3,4,9,10-tetracarboxylic dianhydride (PTARG) as a seeding promoter, as schematized in **Figure 1**a (details in Experimental Section). PTARG acts as a molecular seeding promoter that aids in controlling the kinetic of WS$_2$ growth during the CVD process and assures the formation of large area and thickness-controlled WS$_2$ flakes. The role of the promoter is to increase the wettability of the substrate in a competition of different energetic terms, like the energy of formation of the layers and the interfacial energy between the layers and the substrate. Theoretical and experimental studies demonstrated that this effect is obtained by providing preferential sites for atom adsorption to the surface,[31] thus resulting in an increased adhesion energy of the layers even in the presence of rough substrates.[32] A typical Raman spectrum reported in Figure 1b shows the characteristic phonon modes E$^1_{2g}$(M), 2LA(M)+E$^1_{2g}$(Γ), and A$_{1g}$(Γ) of WS$_2$, with respective frequencies of 321, 349, and 420 cm^{-1}. The map of the intensity ratio I$_{2LA}$/I$_{A1g}$ > 2 (for the 514 nm excitation laser) reported in Figure 1c reveals that flakes thickness is monolayer[33] (Additional Raman and X-ray photoemission spectroscopy data are reported in Figures S1–S3, Supporting Information).

In WS$_2$, the transition from an indirect to a direct bandgap occurring from bulk to the monolayer regime facilitates radiative recombination of excitons, resulting in high photoluminescence

**ADVANCED
SCIENCE NEWS**

www.advancedsciencenews.com

**ADVANCED
FUNCTIONAL
MATERIALS**

www.afm-journal.de

Figure 2. Time and power-dependent PL investigation of WS_2 flakes. a) Evolution of the PL intensity under 1.4 mW μm^{-2} excitation density for 10 s. The inset shows that no PL increase is recorded for the first 0.5 s, probably due to the initial laser-induced desorption of residually adsorbed molecules (see Figure S7, Supporting Information). b) $\Delta PL = PL_i - PL_0$ (where PL_i represents the intensity observed at a given instant and PL_0 is that of the initial time) as a function of time reported for different laser power between 0.1 and 1.4 mW μm^{-2}. c) Scheme of the laser-induced desorption/absorption process over WS_2 surface. d) PL spectra variation as a function of irradiation time in a continuous wave regime at 0.9 mW μm^{-2}. e) Integrated PL intensity of X^0 (red squares) X^T (green circles) and LES (blue triangles). In the lower panel the ratio X^0/X^T is also reported as a function of time. f) Evolution of PL spectrum recorded in a pulsed wave regime at low irradiation intensity (0.1 mW μm^{-2}). g) Integrated PL intensity of X^0 (red squares) X^T (green circles) and LES (blue triangles) observed during the pulsed wave regime. The lower panel reports the variation of X^0/X^T in time.

(PL) with remarkable quantum yield (≈6%) even compared with other transition metal dichalcogenides, like MoS_2 (≈0.1%).[34–36] Figure 1d shows the typical PL spectrum of monolayer WS_2, characterized by a prominent peak at ≈1.98 eV.[34] This spectrum can be deconvoluted into three Gaussian components associated with the presence of excitons (X^0), trions (X^T), and localized states at lower energy (LES). Despite the PL intensity shows high homogeneity over areas of several tens of square micrometers (Figure 1e), regions of higher PL intensity can be observed at the grain boundaries of the WS_2 flake (Note S1, Supporting Information).

2.2. Adaptive Photoluminescent Response of the 2D Memitter

WS_2 exhibits an adaptive PL response that depends on the optical stimulation. Under continuous optical stimulation through laser irradiation, an increase of the PL intensity over time can be observed (**Figure 2a**). As reported in Figure 2b, a more pronounced increase of PL can be noticed by increasing the laser power density. This behavior can be ascribed to laser-induced adsorption of various molecules on the WS_2 surface leading to

an enhancement of its PL response. Indeed, it was previously demonstrated that laser irradiation can favor the adsorption of O_2 and H_2O present in the air,[37] as schematized in Figure 2c. It has been postulated that this process leads to an overall reduction in the n-doping of WS_2 due to electron transfer to the adsorbed molecules with consequent enhancement of the PL intensity (Note S2, Supporting Information). Experiments performed in controlled atmosphere confirm the influence of PL behavior over the environmental conditions (see Figure S6, Supporting Information).

In this context, the specific irradiation scheme (520 nm laser wavelength and power density between 0.1 and 1.4 mW μm^{-2}) does not appear to produce structural photo-damage or degradation, which is typically associated with a progressive decrease in PL intensity over time (Note S3 and Figure S12, Supporting Information). More in detail, the spectral shape undergoes minor variations over time, primarily due to the change of the relative contribution of excitonic and trionic states that induces a slight blue-shift in the total PL spectrum (Figure 2d). While the integrated intensity increase corresponding to X^T and LES is consistent with the absorption of both O_2 and H_2O molecules, the decrease of X^0 dynamics observed after 20 s can be attributed

to a competitive mechanism between the two adsorbates (upper panel in Figure 2e). Initially, the relative weight of X^0 and X^T is essentially balanced ($X^0/X^T \sim 1$). However, interestingly, after the first 10 s of excitation, the X^T contribution is enhanced, reaching a minimum value of $X^0/X^T = 0.5$ (lower panel in Figure 2e). As reported in Figure S8 (Supporting Information), by replicating the PL intensity measurement even after an extended timeframe, it becomes feasible to substantiate the temporal stability of the described behavior.

Results show that changes in the PL intensity of the monolayer WS_2 are reversible and the initial PL response of the monolayer WS_2 can be restored after potentiation, in the present case the prolonged exposure to laser irradiation. Indeed, after the optical stimulation, the PL signal tends to spontaneously relax over time towards the initial PL intensity as shown in Figure 2f. Here, a decrease in the PL over a timescale of hundreds of seconds can be observed (upper panel of Figure 2g). Note that in this case the PL response was monitored by means of laser pulses with duration $t = 100$ ms at 0.1 mW μm^{-2} applied to the sample after a delay time $\Delta t = 20$ s, with the aim of observing the spontaneous PL evolution upon stimulation/over time while minimizing laser-induced PL variations (details in Experimental Section). In these terms, the monolayer WS_2 acts as an emitter with memory, i.e., a 2D memitter.

2.3. Short-Term Synaptic Dynamics

The observed adaptive behavior of the PL response in the 2D material can be exploited for mimicking typical features of biological synapses which regulate synaptic communication and information processing in the nervous system, as schematized in **Figure 3a**. The 2D memitter potentiation under stimulation and subsequent spontaneous relaxation can emulate short-term plasticity (STP), a feature of biological synapses that regulates processing and encoding of information in biological neural networks.[38,39] Figure 3b reports a typical STP characteristic of the 2D memitter, showing potentiation during continuous wave stimulation (CW) and subsequent spontaneous relaxation monitored in pulsed wave (PW) regime (additional data on the effect of pulse length duration on the PL response can be found in Figure S10, Supporting Information). By comparison with the biological systems, the PL response of the device, based on the internal state of the memitter, represents the synaptic weight, where the synaptic dynamics depends on the history of the applied stimulation. For this reason, the experimental data can be well interpolated by a model based on a potentiation-depression rate balance equation.[40,41] This modelling approach relies on describing dynamics of the internal memory state through memory state equation $\frac{dg}{dt} = k_P (1-g) - k_D g$ where g is the normalized memory state of the memitter while k_P and k_D are the potentiation and depression rate coefficients, respectively, that exponentially depend on the applied laser power density. This equation can be solved analytically through an implementable recursive method (details in Experimental Section). Besides well interpolating experimental data, this approach allows to model the dynamics of the internal memory state even in absence of any external stimulation (lower panel of Figure 3b; details in Figure S9, Supporting Information).

These short-term dynamics in 2D memitters can be exploited to emulate typical STP behaviors in biological synapses such as pulse-paired facilitation (PPF). In biological systems, PPF refers to the ability of a synapse to exhibit an enhanced transmission of information in response to timely correlated stimuli, regulating neuronal signaling and synaptic strength modulation.

This can be replicated in the 2D memitter where the stimulation with paired pulses applied within a short-interval results in a gradual increase of PL, as shown by the excitatory postsynaptic (PL) intensity (EPSI) graphic in Figure 3c. As a consequence of the competition between potentiation during pulses and spontaneous relaxation in the delay time Δt in between pulses with duration t, a higher increase of PL can be observed by highly temporally correlated optical pulses while almost negligible changes can be observed in temporally distant pulses, as shown by the PPF index reported in Figure 3d (details in Experimental Section and Figure S10, Supporting Information). As reported in Figure 3e,f, this behavior results in an increase of the PL intensity of the 2D memitter by increasing the frequency of input pulse trains, thus showing that the memitter can be exploited for temporal processing of information. To further highlight the capability of this physical substrate of temporally processing the input signal, the evolution of the system when stimulated with 50 ms while varying the waiting time in between pulses (Δt) is reported in Figure 3g. Also in this case highly correlated input signals are responsible for a higher change in the PL response, as shown also in Figure 3h. For the sake of completeness, we report in Figure 3i the synaptic response of the device by changing the frequency of a square wave stimulation, with frequencies ranging from 10 to 0.33 Hz. All these results show the possibility to tune the device synaptic PL response (and the high-pass temporal filter behavior)[42] by changing the device pulse length as well as the waiting time in between pulses (additional data highlighting the effect of pulse frequency and pulse intensity can be found in Figures S11 and S12, Supporting Information). Notably, the timescales of potentiation/relaxation, spanning from milliseconds to seconds, align with those commonly associated with short-term plasticity effects observed in biological systems.[43,44]
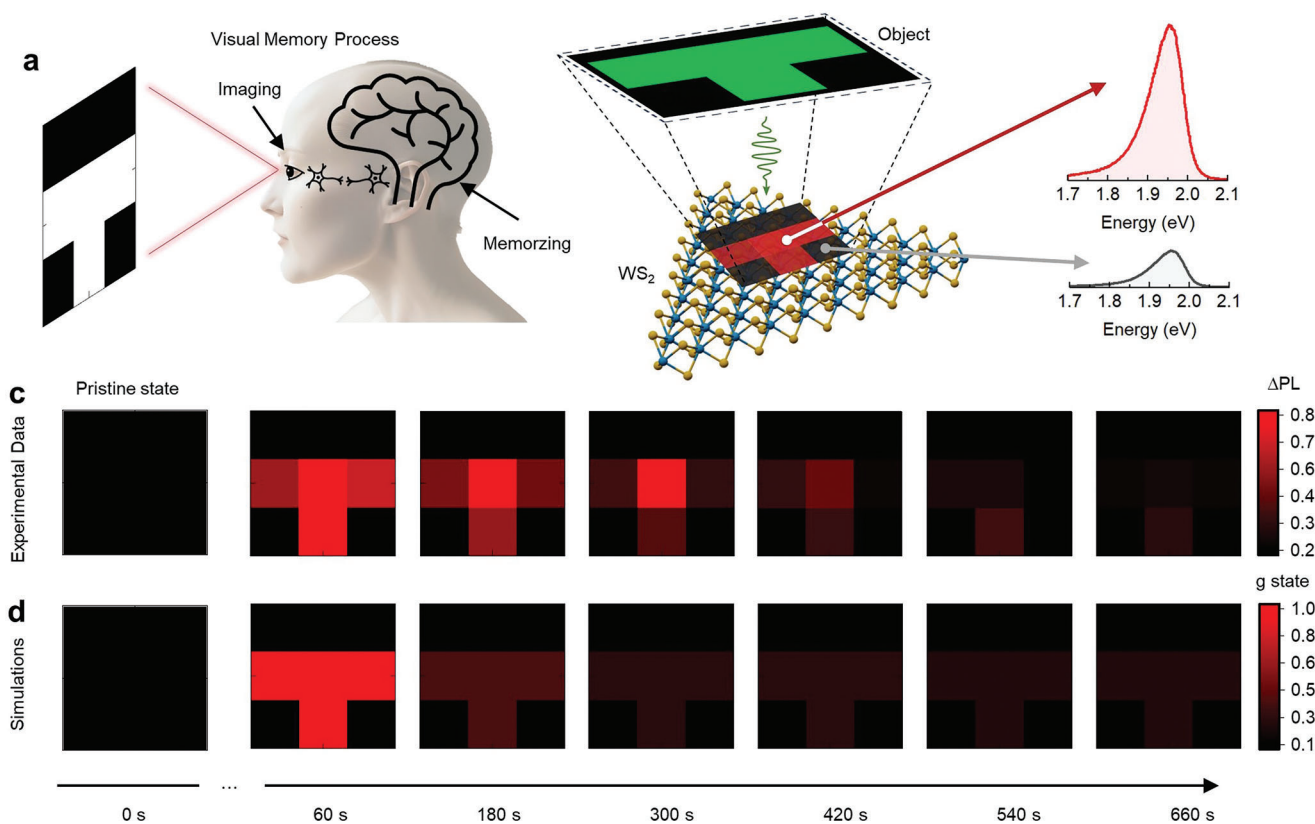
The short-term memory effect related to the temporary storage of information over time represents a crucial aspect for bio-inspired processing of information. Indeed, the interplay between the memorization effect (i.e., the progressive enhancement of the PL of WS_2 during light-induced stimulation) and the forgetting effect (i.e., the spontaneous relaxation of the PL response towards the ground state over time when not stimulated) can be exploited for temporal processing of input signals, exploiting the dependence of the competitive memorization and forgetting mechanisms on the temporal sequence and temporal correlations of input stimuli. Similar memorization-forgetting effects, based on a different physical mechanism based on ionic dynamics, have been exploited for neuromorphic-type of data processing and for neuromorphic computing in memristive devices.[29,45,46]

2.4. Spatio-Temporal Dynamics and Visual Memory

Besides being able to temporally process the optical input signal, the 2D memitter allows processing information also in the spatial domain. This is achieved by spatially modifying the synaptic
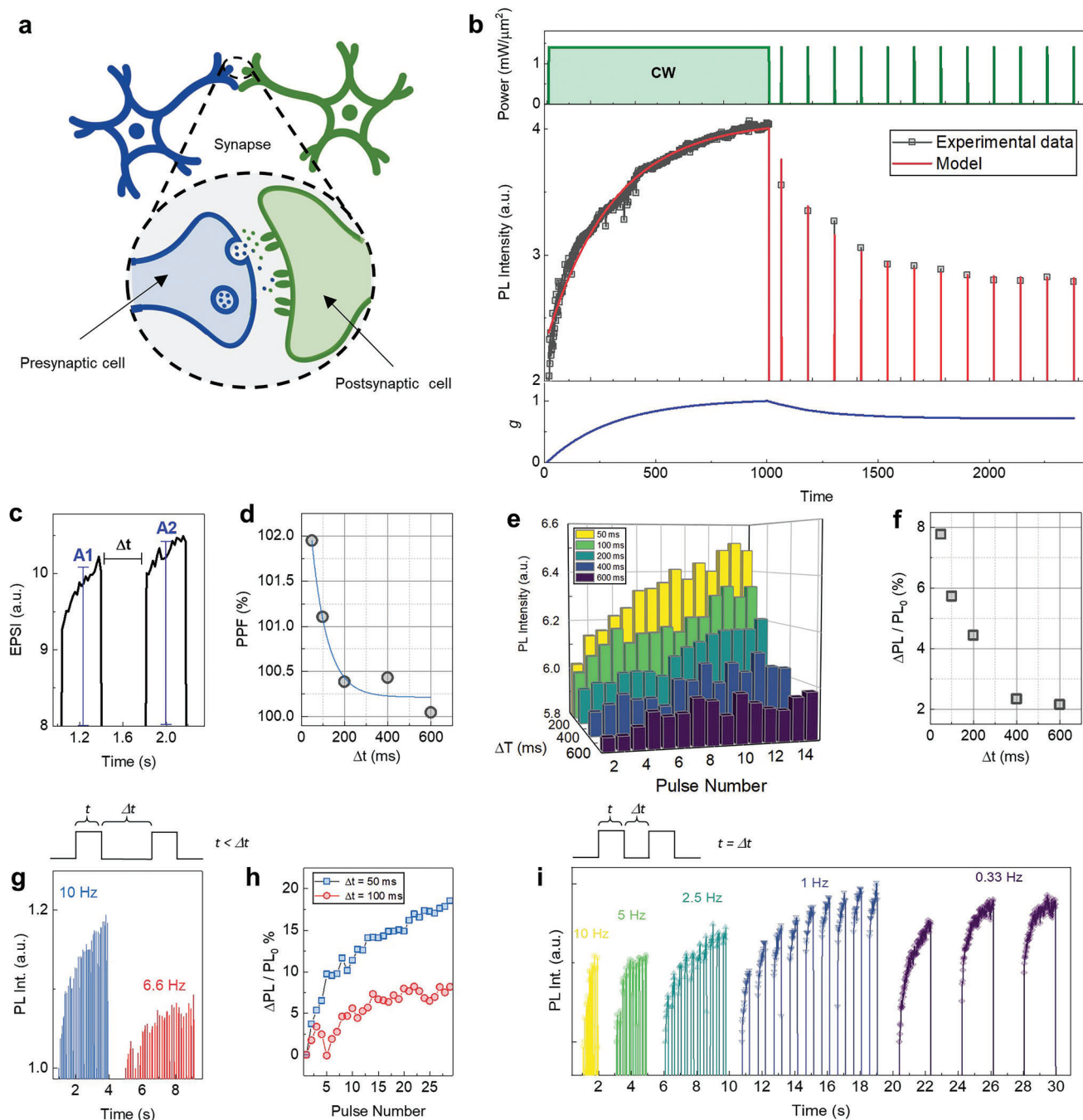
Figure 3. Optical characterization of a WS_2-based 2D memitter. a) Schematic of a biological synapse model, in which presynaptic and postsynaptic cells are separated by a nanometric cleft. Upon receiving stimuli, the presynaptic terminal releases the transmitters towards the postsynaptic terminals. The postsynaptic membrane owns numerous neurotransmitter receptors that have the potential to respond to the released transmitters, thereby facilitating the postsynaptic response. b) Top panel represents the excitation scheme, consisting in a CW writing process (1000 s at 1.4 mW μm^{-2}) followed by pulsed reading (12 pulses of t = 500 ms and Δt = 120 s). The central panel reports the experimental data (black dots) overlapped on the model curve based on the potentiation-depression rate balance equation (red line). In the bottom panel is reported the evolution of the WS_2 memitter memory state g (normalized) as a function of time. c) Excitatory postsynaptic PL after two pulses taken at a delay time of Δt = 400 ms. d) To quantify the PPF in the 2D memitter, light pulses (t = 500 ms) ranging from Δt = 50 ms to 600 ms were applied. The solid blue line is a guide to the eye. e) Percentage increase in PL ($\Delta PL = PL_i - PL_0$), normalized to the intensity of the first pulse (PL_0), as a function of Δt and pulse number. f) Variation of the normalized ΔPL of the last pulse as a function of Δt. g) PL response over 30 potentiation pulses having pulse duration t = 50 ms and Δt = 50 ms (blue line) and Δt = 100 ms (red line), respectively corresponding to frequencies of 10 Hz and 6.6 Hz. h) Normalized PL percentage increase obtained for Δt = 50 ms (blue squares) and 100 ms (red circles). i) PL intensity response observed upon optical excitation using pulses with t = Δt and different pulse duration between 50 and 2000 ms.

ADVANCED
SCIENCE NEWS

www.advancedsciencenews.com

ADVANCED
FUNCTIONAL
MATERIALS

www.afm-journal.de

Figure 4. Visual memory in a 2D memitter. a) Schematic of the optical-visual memory arrays used for mimicking the VSTM behavior. In the VSTM process, visual information from the environment is captured by the imaging system. The brain processes this information and encodes it into a representational format that can be temporarily memorized and afterwards forgotten. b) Graphic representation of the 2D memitter optical excitation forming a T-shaped pattern and PL intensity profiles after stimulation (red spectrum) and without stimulation (black spectrum). c,d) Experimental data (c) and simulations (d) showing visual memory process with the pattern reported in panel (b) in a timescale of minutes.

PL response of different areas of the 2D materials by means of input optical patterns. The spatio-temporal information processing capabilities allow to emulate typical features of the visual system such as Visual Short-Term Memory (VSTM) that plays a crucial role in human perception of external stimuli and encompass both imaging and memory components.[47] In the biological system, VSTM allows temporary storage of visual information in the service of ongoing cognitive tasks, representing the visual storage component of the working memory system.[48,49] A proof of concept demonstration of VSTM in a 2D memitter enabling both image sensing and preservation of relevant information after removing the stimuli, i.e., memory, is conceptually schematized in **Figure** 4a. For this purpose, an optical input pattern of 3×3 pixels is applied to a 3×3 μm^2 area of the 2D memitter (Figure 4b), where red pixels represent stimulation with a 2 mW μm^{-2} power density while black pixels represent no stimulation (details of optical pattern stimulation in Experimental Section and Figure S5, Supporting Information). This turns out in a selective increase of PL in irradiated areas and to almost negligible changes in other non-irradiated areas, as reported in Figure 4b. The experimental implementation of VSTM of the 2D memitter after pattern stimulation is reported in Figure 4c. Here it is possible to observe that the 2D memitter can sense the image pattern thanks to the enhancement of the PL response in stimulated areas and,

at the same time, can preserve the sensed information over time because of its short-term memory capability. Indeed, the stored pattern tends to fade away with a timescale of seconds, similar to the VSTM timescale of biological systems.[48] Experimental results are in good agreement with modelling results reported in Figure 4d reporting the memory state of the 2D memitter in a timescale of minutes.

3. Conclusion and Outlook

Results show that the optically driven reversible tuning of PL of large-area WS_2 can be used for fully optical implementation of neuromorphic functionalities, including typical features of short-term synaptic plasticity and visual memory. Noticeably, the 2D memitter exploits the intrinsic physical properties of the WS_2 directly on the growth substrate without the need of transferring the 2D material, a typical limiting process step usually required for the realization of 2D-based devices, and does not require any lithographic step and/or cleanroom facilities. In this context, the here reported CVD growth technique, based on the use of the seeding promoters, allows for the growth of large-area and monolayer-thick flakes avoiding mechanical exfoliation from bulk crystals, even if the presence of grain boundaries with enhanced PL signal can be deemed as a further de-

gree of freedom in the device engineering. The combined experimental/modeling approach revealed that the stimuli-responsive PL of the 2D memitter based on large WS$_2$ flakes is characterized by *i)* highly nonlinear dynamics, *ii)* fading memory characteristics related to the STP, *iii)* large-area synaptic response. These properties allow for spatio-temporal processing of the input signal, where different areas of the 2D material can process different inputs in parallel (spatial domain) while the response of each area depends on the history of stimulation (temporal domain). These characteristics make the 2D memitter a stable (two years functioning is demonstrated) computing platform for spatio-temporal processing of information in the field of physical reservoir computing, an emerging computational framework that leverages physical phenomena of dynamical systems for cost-efficient computing with low training costs (details in Note S4, Supporting Information).[50,51] In addition, the capability of the 2D memitter to sense, process, and store in the same physical substrate the incoming optical information makes the 2D memitter a candidate for in-sensor computing at the nanoscale. In this context, the realization of an all-optical synapse, where both input and output signals are optical, offers distinct advantages over optoelectronic or purely electronic neuromorphic systems. With respect to the optoelectronic counterpart, key advantages include spatially continuous response (eliminating the need for discretization of input images), seamless image processing (with resolution determined solely by the stimulating laser's spot size), simplified fabrication process and immunity to electrical interference.

In perspective, the here reported concept of 2D memitter can be introduced into a technological process flow by improving the lateral size of the deposited films (ideally to the wafer scale) and by boosting the quantum yield via interface engineering[52] or chemical methods,[53] thus aiming at expanding the matrix dimensions for VSTM applications by considering physical properties of other monolayer materials or intriguing combination of them in the heterostructure fashion,[54] where the spatial resolution of processable input patterns projected on the 2D material relies only on the laser spot size (Figure S5, Supporting Information). Furthermore, the rational design of 2D memitters can be developed by controlling and tuning the synaptic response by environmental conditions, laser excitation energy and power density. The here reported device concept can further stimulate new concepts for the realization of novel neuromorphic systems based on 2D materials, towards the realization of bio-inspired intelligent systems at the nanoscale that exploit optical processing of information.

4. Experimental Section

WS$_2$ Synthesis: The synthesis of WS$_2$ crystals was carried out in a CVD reactor based on a hot-wall furnace and a 1-inch diameter fused quartz tube. Alumina boat containing a mixture of 35 mg WO$_3$ (99.9%, Sigma-Aldrich) and 5 mg NaCl (>99%, Sigma-Aldrich) powders was loaded in the center of the tube, while the growth substrates, SiO$_2$ (50 nm)/Si^{++}, was placed ≈10 mm above the powders with the polished face down. Another boat containing ≈100 mg of S powder (99.98%, Merck) was placed in the upstream region of the quartz tube. Before loading in the CVD apparatus, the substrates were cleaned in three different steps: 5 min in acetone, 5 min in isopropanol, 5 min washed in deionized (DI) water. Subsequently,

the substrates were dried by means of a nitrogen flux. A solution of seeding promoter was used to condition the SiO$_2$ substrate. The seeding promoter was the PTARG dissolved in DI water. Perylene-3,4,9,10-tetracarboxylic dianhydride (1.3 mmol) was combined with imidazole (29 mmol) under vigorous stirring at a temperature of 110 °C. Following this, arginine methyl ester dihydrochloride (1.8 mmol) was added to the mixture and stirred intensely for a duration of 4 h. As the reaction proceeded, a dark red solid precipitated, prompting the cooling of the reaction mixture. To remove the imidazole, the precipitate was washed multiple times with methanol. Ultimately, a dark red solid product was obtained with a yield of 75%. PTARG (0.37 mg) mixed in 10 mL distilled water was used to obtain a 50 μM L^{-1} solution. The solution was spread on the substrate (surface of 2 cm^2) by delivering 10 drops of solution (≈50 mg) using a pipette. The CVD growth is carried out by heating the furnace up to 850 °C at a rate of 10 °C min and with a carrier gas (H$_2$/Ar, 4% vol. H$_2$) flux of 0.2 L h^{-1}.

Raman Spectroscopy: Raman spectroscopy measurements were performed using 514 (2.41) and 532 nm (2.33 eV) excitation wavelengths. In the first case a backscattering configuration equipped with a 514 nm line of solid-state diode laser was used. The laser radiation was focused on the sample by means of a 50× objective (0.75 numerical aperture). In the second case data were acquired using a Witec Gmbh Alpha300AR fiber coupled confocal Raman (70 mW @ 532 nm laser excitation, 600 and 1800 g mm^{-1} Ultrahight Throughput spectrometer with a Peltier cooled Newton EMCCD camera), using a 100× objective (Zeiss EC Epiplan Neofluar 0.90 numerical aperture) capable to perform spectral mapping. 170 × 170 μm^2, 32 × 32 points maps were acquired using an excitation power <1 mW to avoid photodamage and an integration time of 4 s for each single spectrum.

Pulsed Experiments: The pulsed regime experiments were conducted in the same measurement setup employed for continuous PL measurements (520 nm wavelength, see description in Figure S4, Supporting Information), with the excitation laser modulated using variable activation and deactivation times ranging from 50 to 1000 ms (see Figure S10, Supporting Information). As a result, the EPSI triggered by the second pulse was larger than that of the first one. In Figure 3d the increase PPF index, defined as (A$_2$ / A$_1$) × 100, where A$_1$ and A$_2$ represent respectively the PL intensity of the first and second pulse, was plotted as a function of Δt (Figure 3c), with a maximum value of 102% for Δt = 50 ms. Experiments were carried out in ambient with controlled temperature and humidity (21 °C and 40%, respectively).

2D Memitter Excitation: To excite the T-shaped pattern discussed in Figure 4 a WS$_2$ flake showing a sufficiently large homogeneous area (larger than 20 × 20 μm^2) in terms of PL emission (see Figure S9f, Supporting Information) was used. Mirror L1 (see Figure S3, Supporting Information for the setup description) was then moved to the focusing configuration and stimulated 4 different points separated by 10 μm by illuminating each point for 10 s with power density 2 mW μm^{-2}.

To monitor the PL intensity decay in time mirror L1 was moved to the defocusing position and acquired a PL wide field image every minute for 0.5 s at 0.5 μW μm^{-2}.

The frames acquired by the CMOS camera were analyzed as follows for the reading procedure: before the excitation a frame was acquired in the defocusing configuration used as PL background signal. From the 20 × 20 μm^2 luminescent region 9 areas roughly 1 × 1 μm^2 were selected over which the average PL intensity was computed for each reading frame, after removing the PL background intensity. The areas were separated by 10 μm in x and y directions on the plane and chosen so that the 4 excited spots correspond to 4 of the 9 analyzed regions.

XPS: The micro X-Ray Photoelectron Spectroscopy (μXPS) analysis was carried out using a PHI 5000 Versaprobe Scanning X-ray Photoelectron Spectrometer (Physical ElectronicsChanhassen, MN, USA), adopting monochromatic Al Kα radiation (1486.6 eV) as an X-ray source, at 15 kV voltage and 1 mA anode current. The working pressure reached a maximum value inside the main chamber of 10^{-6} Pa.

Modeling: The here proposed modeling approach was adapted from a model originally developed to describe short-term dynamics of memristive devices.[36] In this framework, it was assumed that the PL response of the device can be described by the equation:

**ADVANCED
SCIENCE NEWS**

www.advancedsciencenews.com

**ADVANCED
FUNCTIONAL
MATERIALS**

www.afm-journal.de

$$PL_{intensity} = [PL_{min} (1 - g) + PL_{max} g] \cdot S \tag{1}$$

where g is the memory state of the device (that can assume values between 0 and 1), while PL_{min} and PL_{max} are the minimum and maximum PL values of the memitter, and S the laser power density. Note that this equation implies the assumption of a linear dependence of the PL response to the laser power (Figure S7m, Supporting Information). The memory state equation describing STP is expressed through the equation:

$$\frac{dg}{dt} = k_P (1 - g) - k_D g \tag{2}$$

where k_P and k_D are the potentiation and depression rate coefficient, respectively. It was assumed k_P and k_D have an exponential relationship with the applied laser power density (S) according to the relationships:

$$k_P (S) = k_{P0} \, e^{(\eta_P \, S)} \tag{3}$$

$$k_D (S) = k_{D0} \, e^{(\eta_D \, S)} \tag{4}$$

where k_{P0} and k_{D0} are constants while η_P and η_D represent the transition rates. This equation can be iteratively solved as:

$$g_t = \frac{k_P}{k_P + k_D} \left\{ 1 - \left[1 - \left(1 + \frac{k_D}{k_P} \right) g_{t-1} \right] e^{-(k_P + k_D)\Delta t} \right\} \tag{5}$$

where g_t and g_{t-1} are the normalized memory states at times t and t-1, respectively. Note that this solution allows to simulate the memitter response to arbitrary optical inputs, including optical pulses. Modelling results reported in Figure 4d, where the relaxation of previously irradiated pixels have been modelled with Equation (2), have been obtained by interpolating the PL response of a representative pixel of the pattern reported in Figure 4c.

Supporting Information

Supporting Information is available from the Wiley Online Library or from the author.

Acknowledgements

Conflict of Interest

The authors declare no conflict of interest.

Data Availability Statement

The data that support the findings of this study are available in the supplementary material of this article.

[1] D. V. Christensen, R. Dittmann, B. Linares-Barranco, A. Sebastian, M. Le Gallo, A. Redaelli, S. Slesazeck, T. Mikolajick, S. Spiga, S. Menzel, I. Valov, G. Milano, C. Ricciardi, S.-J. Liang, F. Miao, M. Lanza, T. J. Quill, S. T. Keene, A. Salleo, J. Grollier, D. Marković, A. Mizrahi, P. Yao, J. J. Yang, G. Indiveri, J. P. Strachan, S. Datta, E. Vianello, et al., *Neuromorphic Comput. Eng.* **2022**, *2*, 022501.

[2] D. Marković, A. Mizrahi, D. Querlioz, J. Grollier, *Nat. Rev. Phys.* **2020**, *2*, 499.

[3] H. Jaeger, B. Noheda, W. G. van der Wiel, *Nat. Commun.* **2023**, *14*, 4911.

[4] D. Ham, H. Park, S. Hwang, K. Kim, *Nat. Electron.* **2021**, *4*, 635.

[5] B. J. Shastri, A. N. Tait, T. Ferreira de Lima, W. H. P. Pernice, H. Bhaskaran, C. D. Wright, P. R. Prucnal, *Nat. Photonics* **2021**, *15*, 102.

[6] W. Zhang, B. Gao, J. Tang, P. Yao, S. Yu, M.-F. Chang, H.-J. Yoo, H. Qian, H. Wu, *Nat. Electron.* **2020**, *3*, 371.

[7] T. Wan, B. Shao, S. Ma, Y. Zhou, Q. Li, Y. Chai, *Adv. Mater.* **2022**, *35*, 2203830.

[8] F. Zhou, Y. Chai, *Nat. Electron.* **2020**, *3*, 664.

[9] D. Lee, M. Park, Y. Baek, B. Bae, J. Heo, K. Lee, *Nat. Commun.* **2022**, *13*, 5223.

[10] Z. Wang, H. Wu, G. W. Burr, C. S. Hwang, K. L. Wang, Q. Xia, J. J. Yang, *Nat. Rev. Mater.* **2020**, *5*, 173.

[11] M.-K. Song, J.-H. Kang, X. Zhang, W. Ji, A. Ascoli, I. Messaris, A. S. Demirkol, B. Dong, S. Aggarwal, W. Wan, S.-M. Hong, S. G. Cardwell, I. Boybat, J. Seo, J.-S. Lee, M. Lanza, H. Yeon, M. Onen, J. Li, B. Yildiz, J. A. del Alamo, S. Kim, S. Choi, G. Milano, C. Ricciardi, L. Alff, Y. Chai, Z. Wang, H. Bhaskaran, M. C. Hersam, et al., *ACS Nano* **2023**, *17*, 11994.

[12] V. K. Sangwan, M. C. Hersam, *Nat. Nanotechnol.* **2020**, *15*, 517.

[13] G. Cao, P. Meng, J. Chen, H. Liu, R. Bian, C. Zhu, F. Liu, Z. Liu, *Adv. Funct. Mater.* **2021**, *31*, 2005443.

[14] J. Zhu, Y. Yang, R. Jia, Z. Liang, W. Zhu, Z. U. Rehman, L. Bao, X. Zhang, Y. Cai, L. Song, R. Huang, *Adv. Mater.* **2018**, *30*, 1800195.

[15] T. Paul, T. Ahmed, K. Kanhaiya Tiwari, C. Singh Thakur, A. Ghosh, *2d Mater.* **2019**, *6*, 045008.

[16] K. Liu, B. Dang, T. Zhang, Z. Yang, L. Bao, L. Xu, C. Cheng, R. Huang, Y. Yang, *Adv. Mater.* **2022**, *34*, 2108826.

[17] A. I. Khan, A. Keshavarzi, S. Datta, *Nat. Electron.* **2020**, *3*, 588.

[18] L. Chen, L. Wang, Y. Peng, X. Feng, S. Sarkar, S. Li, B. Li, L. Liu, K. Han, X. Gong, J. Chen, Y. Liu, G. Han, K. Ang, *Adv. Electron. Mater.* **2020**, *6*, 2000057.

[19] V. K. Sangwan, D. Jariwala, I. S. Kim, K. S. Chen, T. J. Marks, L. J. Lauhon, M. C. Hersam, *Nat. Nanotechnol.* **2015**, *10*, 403.

[20] V. K. Sangwan, H. S. Lee, H. Bergeron, I. Balla, M. E. Beck, K. S. Chen, M. C. Hersam, *Nature* **2018**, *554*, 500.

[21] Y. Shi, X. Liang, B. Yuan, V. Chen, H. Li, F. Hui, Z. Yu, F. Yuan, E. Pop, H.-S. P. Wong, M. Lanza, *Nat. Electron.* **2018**, *1*, 458.

[22] W. Huh, D. Lee, C. Lee, *Adv. Mater.* **2020**, *32*, 2002092.

[23] K. Zhu, S. Pazos, F. Aguirre, Y. Shen, Y. Yuan, W. Zheng, O. Alharbi, M. A. Villena, B. Fang, X. Li, A. Milozzi, M. Farronato, M. Muñoz-Rojo, T. Wang, R. Li, H. Fariborzi, J. B. Roldan, G. Benstetter, X. Zhang, H. N. Alshareef, T. Grasser, H. Wu, D. Ielmini, M. Lanza, *Nature* **2023**, *618*, 57.

**ADVANCED
SCIENCE NEWS**

www.advancedsciencenews.com

**ADVANCED
FUNCTIONAL
MATERIALS**

www.afm-journal.de

[24] L. Mennel, J. Symonowicz, S. Wachter, D. K. Polyushkin, A. J. Molina-Mendoza, T. Mueller, *Nature* **2020**, *579*, 62.

[25] K. Liu, T. Zhang, B. Dang, L. Bao, L. Xu, C. Cheng, Z. Yang, R. Huang, Y. Yang, *Nat. Electron.* **2022**, *5*, 761.

[26] H. Bian, X. Qin, Y. Wu, Z. Yi, S. Liu, Y. Wang, C. D. S. Brites, L. D. Carlos, X. Liu, *Adv. Mater.* **2022**, *34*, 2101895.

[27] H. Wang, Y. Zhang, C. Zhou, X. Wang, H. Ma, J. Yin, H. Shi, Z. An, W. Huang, *Light: Sci. Appl.* **2023**, *12*, 90.

[28] J. H. Kang, H. Shin, K. S. Kim, M. K. Song, D. Lee, Y. Meng, C. Choi, J. M. Suh, B. J. Kim, H. Kim, A. T. Hoang, B. I. Park, G. Zhou, S. Sundaram, P. Vuong, J. Shin, J. Choe, Z. Xu, R. Younas, J. S. Kim, S. Han, S. Lee, S. O. Kim, S. Kang, S. Seo, H. Ahn, S. Seo, K. Reidy, E. Park, S. Mun, et al., *Nat. Mater.* **2023**, *22*, 1470.

[29] Z. Wang, S. Joshi, S. E. Savel'ev, H. Jiang, R. Midya, P. Lin, M. Hu, N. Ge, J. P. Strachan, Z. Li, Q. Wu, M. Barnell, G. L. Li, H. L. Xin, R. S. Williams, Q. Xia, J. J. Yang, *Nat. Mater.* **2017**, *16*, 101.

[30] S. Li, S. Wang, D.-M. Tang, W. Zhao, H. Xu, L. Chu, Y. Bando, D. Golberg, G. Eda, *Appl. Mater. Today* **2015**, *1*, 60.

[31] H. Ko, H. S. Kim, M. S. Ramzan, S. Byeon, S. H. Choi, K. K. Kim, Y. H. Kim, S. M. Kim, *2d Mater.* **2020**, *7*, 015013.

[32] C. Martella, D. Campi, P. P. Tummala, E. Kozma, P. Targa, D. Codegoni, M. Bernasconi, A. Lamperti, A. Molle, *Nanomaterials* **2022**, *12*, 4050.

[33] A. Berkdemir, H. R. Gutiérrez, A. R. Botello-Méndez, N. Perea-López, A. L. Elías, C.-I. Chia, B. Wang, V. H. Crespi, F. López-Urías, J.-C. Charlier, H. Terrones, M. Terrones, *Sci. Rep.* **2013**, *3*, 1755.

[34] H. R. Gutiérrez, N. Perea-López, A. L. Elías, A. Berkdemir, B. Wang, R. Lv, F. López-Urías, V. H. Crespi, H. Terrones, M. Terrones, *Nano Lett.* **2013**, *13*, 3447.

[35] M. S. Kim, S. J. Yun, Y. Lee, C. Seo, G. H. Han, K. K. Kim, Y. H. Lee, J. Kim, *ACS Nano* **2016**, *10*, 2399.

[36] N. Peimyoo, W. Yang, J. Shang, X. Shen, Y. Wang, T. Yu, *ACS Nano* **2014**, *8*, 11320.

[37] H. Zhang, J. R. Dunklin, O. G. Reid, S. J. Yun, S. U. Nanayakkara, Y. H. Lee, J. L. Blackburn, E. M. Miller, *Nanoscale* **2020**, *12*, 8344.

[38] R. S. Zucker, W. G. Regehr, *Annu. Rev. Physiol.* **2002**, *64*, 355.

[39] C. Li, X. Zhang, P. Chen, K. Zhou, J. Yu, G. Wu, D. Xiang, H. Jiang, M. Wang, Q. Liu, *iScience* **2023**, *26*.

[40] G. Milano, E. Miranda, C. Ricciardi, *Neural Networks* **2022**, *150*, 137.

[41] E. Miranda, G. Milano, C. Ricciardi, *IEEE Trans. Nanotechnol.* **2020**, *19*, 609.

[42] J. K. Qin, F. Zhou, J. Wang, J. Chen, C. Wang, X. Guo, S. Zhao, Y. Pei, L. Zhen, P. D. Ye, S. P. Lau, Y. Zhu, C. Y. Xu, Y. Chai, *ACS Nano* **2020**, *14*, 10018.

[43] A. Citri, R. C. Malenka, *Neuropsychopharmacology* **2008**, *33*, 18.

[44] S. H. Sung, T. J. Kim, H. Shin, T. H. Im, K. J. Lee, *Nat. Commun.* **2022**, *13*, 2811.

[45] G. Milano, M. Luebben, Z. Ma, R. Dunin-Borkowski, L. Boarino, C. F. Pirri, R. Waser, C. Ricciardi, I. Valov, *Nat. Commun.* **2018**, *9*, 5151.

[46] S. Li, M. E. Pam, Y. Li, L. Chen, Y. C. Chien, X. Fong, D. Chi, K. W. Ang, *Adv. Mater.* **2022**, *34*, 2103376.

[47] C. Giotis, A. Serb, V. Manouras, S. Stathopoulos, T. Prodromakis, *Sci. Adv.* **2022**, *8*, abn7920.

[48] J. J. Todd, R. Marois, *Nature* **2004**, *428*, 751.

[49] R. Marois, J. Ivanoff, *Trends Cogn. Sci.* **2005**, *9*, 296.

[50] K. Nakajima, *Jpn. J. Appl. Phys.* **2020**, *59*, 060501.

[51] G. Tanaka, T. Yamane, J. B. Héroux, R. Nakane, N. Kanazawa, S. Takeda, H. Numata, D. Nakano, A. Hirose, *Neural Networks* **2019**, *115*, 100.

[52] Y. Lee, J. D. S. Forte, A. Chaves, A. Kumar, T. T. Tran, Y. Kim, S. Roy, T. Taniguchi, K. Watanabe, A. Chernikov, J. I. Jang, T. Low, J. Kim, *Nat. Commun.* **2021**, *12*, 7095.

[53] K. Chen, S. Deng, E. Chen, S. Wen, T. Ouyang, X. Wang, R. Zhan, J. Cai, H. Chen, *ACS Appl. Mater. Interfaces* **2021**, *13*, 44814.

[54] A. R.-P. Montblanch, M. Barbone, I. Aharonovich, M. Atatüre, A. C. Ferrari, *Nat. Nanotechnol.* **2023**, *18*, 555.

2403158 (9 of 9)